MATERIALS SCIENCE

A biopolymer hydrogel electrostatically reinforced by amino-functionalized bioactive glass for accelerated bone regeneration

Xinxin Ding†, Junyu Shi†, Jianxu Wei, Yuan Li, Xiangbing Wu, Yi Zhang, Xue Jiang, Xiaomeng Zhang*, Hongchang Lai*

Composite hydrogels incorporating natural polymers and bioactive glass (BG) are promising materials for bone regeneration. However, their applications are compromised by the poor interfacial compatibility between organic and inorganic phases. In this study, we developed an electrostatically reinforced hydrogel (CAG) with improved interfacial compatibility by introducing amino-functionalized 45S5 BG to the alginate/gellan gum (AG) matrix. BAG composed of AG and unmodified BG (10 to 100 μm in size) was prepared as a control. Compared with BAG, CAG had a more uniform porous structure with a pore size of 200 μm and optimal compressive strength of 66 kPa. Furthermore, CAG promoted the M2 phenotype transition of macrophages and up-regulated the osteogenic gene expression of stem cells. The new bone formation in vivo was also accelerated due to the enhanced biomineralization of CAG. Overall, this work suggests CAG with improved interfacial compatibility is an ideal material for bone regeneration application.

INTRODUCTION

Bone defects are typically observed in patients with severe trauma, osteitis, or bone tumors. Prolonged hospitalization and increased financial burden both pose a great burden to patients (*1*). However, the efficient repairing of bone defects is still a challenging issue for clinicians (*1*). With the advancement of material science, researchers have increasingly focused on developing new biomaterials to enhance bone regeneration (*2*). Natural biopolymer-based hydrogels have received particular consideration due to their outstanding biocompatibility and biodegradability (*3*). Among various natural polymers, negatively charged alginate and gellan gum (AG) exhibited good potential for clinical applications because they are economically available and easily gelled by adding low concentration of mono- or multivalent cations, such as calcium ions (*4*). Hydrogels composed of AG have been shown to induce satisfactory osteogenesis (*5*). The porous structure of AG exhibited structural similarity with natural bone tissue and provided enough space for early cell attachment and osteogenic differentiation (*5*).

Although several studies have demonstrated the advantages of AG in promoting osteogenesis in vitro as mentioned above (*3*–*5*), the mechanical properties of pure hydrogels are usually insufficient for bone defect repairing in vivo (*6*). Moreover, the osteogenic activity of hydrogels is also limited due to the lack of growth factors (*6*). Alternatively, the development of composite hydrogels by incorporating inorganic particles can largely avoid the disadvantages of pure hydrogels (*7*). Bioactive glass (BG) has been increasingly applied as an inorganic component in composites due to its bone bonding ability and osteogenic and angiogenic properties (*8*). The first developed BG, 45S5 Bioglass [45% SiO_2, 24.5% Na_2O, 24.5% CaO, and 6% P_2O_5, in weight % (wt %)] was developed by Hench *et al.* and has been commercially used for orthopedic and dental treatment (*9*). The incorporation of 45S5 BG to hydrogels has been demonstrated to substantially enhance the mechanical strength and osteogenic activity of natural polymer-based hydrogels (*10*). However, poor interfacial compatibility has been reported between the polymer matrix and inorganic particles, which may lead to the disturbed separation of BG in composite hydrogels and consequently affect their properties (e.g., stability and mechanical behavior) (*11*). Most studies focused on developing new types of organic or inorganic components to acquire enhanced osteogenesis (*12*, *13*). Few efforts have been dedicated to improve the interfacial compatibility between BG and polymer matrices (*14*).

One approach to address this issue is to develop hybrid hydrogels by establishing interfacial bonds between different phases (*15*). Synthesis of hybrids with covalent interfacial bond is complex (*16*). It is also a challenge to incorporate essential ions for osteogenesis into the covalent network (*16*). Thus, noncovalent cross-linking between inorganic fillers and matrices is probably a more practical method for clinical applications. In a previous study, Lee *et al.* (*17*) attempted to establish electrostatic bonds between anionic polymer matrices and cationic silica nanoparticles to prepare a bioprinting hybrid. This hydrogel showed superior structural integrity and interfacial compatibility without sacrificing original properties of each component (*17*). Inspired by this, the formation of electrostatic interaction between polymer matrices and BG may be an ideal way to obtain composite hydrogels with improved interfacial compatibility. Notably, although pure BG particles are negatively charged, a preliminary research indicated that amino-modified BG (NBG) are positively charged particles which are easily obtained and showed better osteogenic ability than nonfunctionalized BG (*18*, *19*).

Hence, in the present study, an electrostatically reinforced hydrogel (CAG) composed of cationic NBG (45S5 composition) and anionic AG was synthesized. Interfacial compatibility was improved by forming electrostatic interactions between organic and inorganic phases. The gelation network of hydrogels was subsequently enhanced by

Department of Oral Implantology, Shanghai Ninth People's Hospital, Shanghai Jiao Tong University School of Medicine; College of Stomatology, Shanghai Jiao Tong University; National Center for Stomatology; National Clinical Research Center for Oral Diseases; Shanghai Key Laboratory of Stomatology, Shanghai, China.
*Corresponding author. Email: hongchanglai@126.com (H.L.); zhangxiaomengwowo@126.com (X.Z.)
†These authors contributed equally to this work.

ionic cross-linking using calcium ions, as shown in Fig. 1. For a control, BAG was fabricated by mixing nonfunctionalized BG and AG. Although composite hydrogels formed by electrostatic interaction have been reported before, the aim of their study was dedicated to create a self-assembled gelation network and obtain hydrogels with enhanced shear-thinning or self-healing ability (*20*, *21*). To the best of our knowledge, the present study is the first attempt to comprehensively compare the different physiochemical properties and osteogenic behavior between composites with improved interfacial compatibility (CAG) and normal composites (BAG). The objectives of this study were to (i) form the CAG hydrogel by forming electrostatic interactions between NBG and AG, (ii) characterize and compare the physiochemical properties of hydrogels, and (iii) investigate the bone regeneration ability of different hydrogels.

RESULTS AND DISCUSSION

Detection of the interfacial interaction in CAG

The preparation of NBG and CAG was shown in Fig. 2A. In contrast to BAG, which was obtained by physical mixing of components, CAG was designed to be an electrostatically reinforced hydrogel with interfacial interaction between phases. The amino groups on NBG surface were expected to react with the carboxyl groups on polymer chains through electrostatic interaction (Fig. 2A) (*22*). X-ray photoelectron spectroscopy (XPS) and zeta potential test were used to investigate the presence of electrostatic interaction in CAG. The grafted amino groups on NBG were first detected by XPS. As shown in Fig. 2B, the spectrum of N1s in NBG was deconvoluted into two components, $-NH_2$ (399.93 eV) and $-NH_3^+$ (401.00 eV), suggesting the successful synthesis of NBG with a positive surface (*23*). A zeta potential test was further conducted to confirm the appearance of electrostatic interactions in CAG (Fig. 2C). The pure polymer matrix in AG was negatively charged, whereas the inorganic NBG exhibited a positive charge. The combination of polymer matrix with NBG may have induced the electrostatic attraction in CAG (*22*).

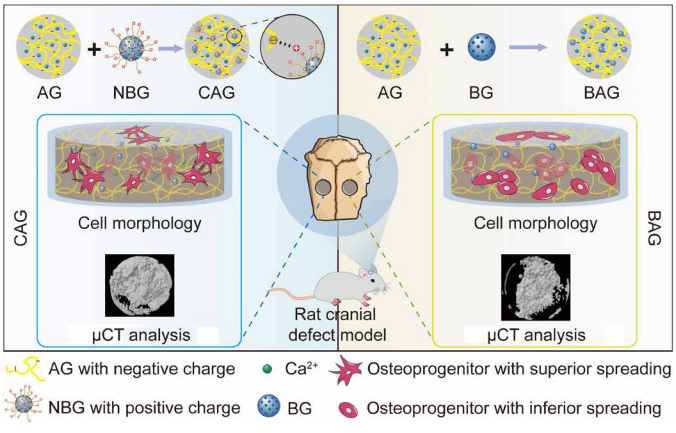

Fig. 1. Preparation and biomedical application of hydrogels. CAG was fabricated by forming electrostatic interaction between cationic NBG and anionic AG. BAG was obtained by simply mixing AG and BG component. A rat cranial bone defect model was used to detect the biocompatibility and osteogenic activity of hydrogels. Cells in CAG exhibited favorable cell spreading, while there was no obvious cell pseudopodium observed in BAG. Moreover, bone regeneration was also enhanced in CAG compared with BAG. micro–computed tomography (μCT).

Structural analysis of hydrogels

Representative Fourier transform infrared (FTIR) spectra for AG, BAG, and CAG are shown in Fig. 2D. The AG spectrum had characteristic bands of polysaccharides, e.g., 1305 and 939 cm^{-1} (C—O stretching), 1147 cm^{-1} (C—C stretching), 1010 cm^{-1} (C—O—C stretching), and a shoulder at 1074 cm^{-1} (C—C and C—O stretching) (*24*). Moreover, bands at 1596 and 1429 cm^{-1} corresponded to the carboxyl group, and a wide stretching peak at 3368 cm^{-1} was assigned to the –OH group (*25*) For BAG and CAG spectra, new bands located at 480, 821, and 1078 cm^{-1} were attributed to the Si—O—Si group (*26*). The wider stretching peak at 3222 to 3388 cm^{-1} in CAG was probably due to the presence of amino groups on NBG (*27*). X-ray diffractometer (XRD) analysis was used to detect potential crystalline phases in hydrogels. As shown in Fig. 2E, the XRD patterns of AG and BAG both exhibited a broad peak centered at ~30° (2θ), suggesting the amorphous state of polymers and BG component. However, CAG showed distinct apatite peaks at 31.56°, 45.54°, and 56.46°, which was probably due to the formation of semicrystalline hydroxyapatite (HA) during the in situ preparation of CAG. The superior bioactivity of NBG may promote the formation of HA on CAG. Compared with the Si—OH groups on BG, the amino groups on NBG have a stronger electrostatic interaction ability with the calcium and phosphate components in solution, which facilitates their use as nucleation points for HA mineralization in the in situ preparation of CAG (*28*). The formed crystallized apatite phase in CAG made the hydrogel osteoinductive at an early time (*28*).

To understand the effect of particles on the hydrogel microstructure, the morphologies of BG and NBG were firstly detected using a scanning electron microscope (SEM). As shown in Fig. 2 (F and G), the particle size of commercial BG (45% SiO_2, 24.5% CaO, 24.5% Na_2O, and 6% P_2O_5, wt %) was variable in a range of 10 to 100 μm, while the size of NBG was uniform and larger. The presence of homogeneous NBG particles may be attributed to the synthetic method. More large and uniform particles precipitated during the centrifugal sedimentation of NBG (*29*). The microstructure morphology of hydrogels was further analyzed by detecting the cross-sectional images using SEM, as shown in Fig. 3 (A to F). The porous surface of AG was smooth, and the pore size was in a range of 50 to 100 μm (Fig. 3, A and D). The incorporation of inorganic particles affected substantially the structural morphology of hydrogels. BAG and CAG both exhibited identical three-dimensional (3D) porous structure (Fig. 3, B and C). The pore size of BAG ranged from 5 to 100 μm, which was smaller than that of CAG. The pores in CAG were homogenous with a diameter of approximately 200 μm (Fig. 3C). The relatively larger pores of CAG facilitate the rapid vascularization and high oxygenation of CAG in vivo, further enhancing bone ingrowth and osseointegration at the bone defect site (*30*). Furthermore, the magnified images indicated that NBG was well-separated into CAG (Fig. 3F). The homogeneous hydrogel surface suggested the optimal compatibility between particles and polymers in CAG (Fig. 3F). In contrast, particle aggregation was observed on BAG surface (Fig. 3E). The ideal microstructure of CAG may probably attributed to the fine scale interaction between different phases (*31*). The electrostatic bonds in CAG ensured good regulation of polymer chains and uniform dispersion of inorganic particles, further contributing to the homogeneous morphology of CAG (*31*). In contrast, the compressed structure of BAG possibly resulted from the agglomeration of BG particles in the composite (*31*).

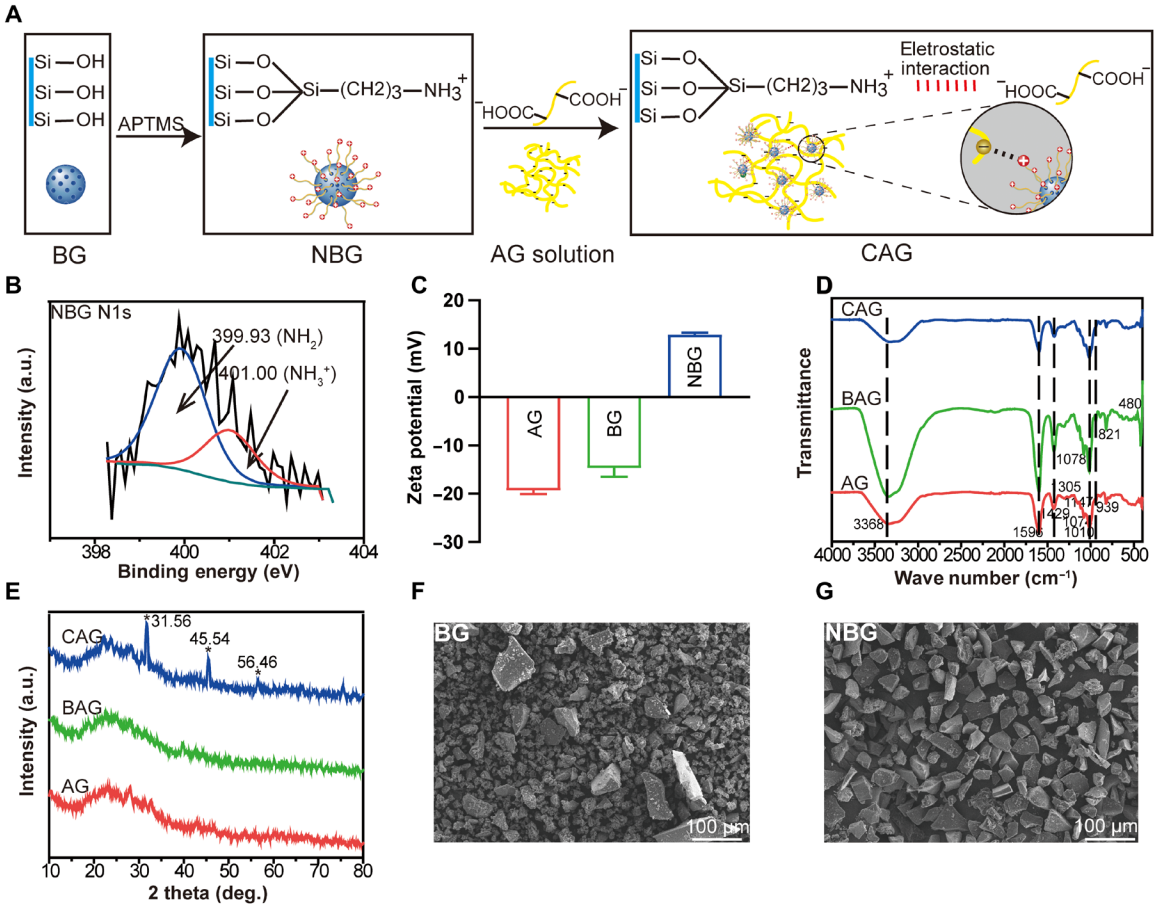

Fig. 2. Structural analysis of synthesized hydrogels. (**A**) Scheme of the preparation of NBG and CAG. APTMS, (3-aminopropyl) trimethoxysilane. (**B**) High-resolution x-ray photoelectron spectroscopy spectra of N1s in NBG particles. a.u., arbitrary units. (**C**) Zeta potential of AG, BG, and NBG. (**D**) Fourier transform infrared spectra of AG, BAG, and CAG. (**E**) X-ray diffractometer patterns of AG, BAG, and CAG. (**F**) Scanning electron microscopy (SEM) image of BG. (**G**) SEM image of synthesized NBG.

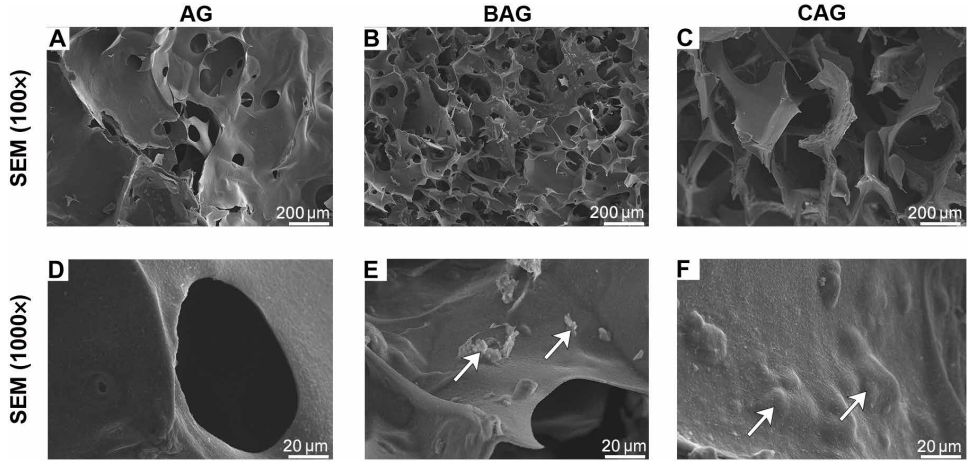

Fig. 3. Cross-sectional images of different hydrogels using SEM analysis. (**A** to **C**) SEM images of AG, BAG, and CAG. (**D** to **F**) Magnified images of AG, BAG, and CAG. White arrows in (E) and (F) indicate the BG and NBG particles on the hydrogel surface.

Physiochemical properties of different hydrogels

The swelling property is one of the most important physical characteristics of hydrogels. Swollen hydrogels promote substance exchange by absorbing nutrients from external environment (*6*). As shown in Fig. 4A, the incorporation of BG significantly decreased the swelling ratio of BAG compared with that of AG ($P < 0.05$). However, the swelling property of CAG was not noticeably affected by the incorporation of NBG. CAG shows even greater water retention capacity

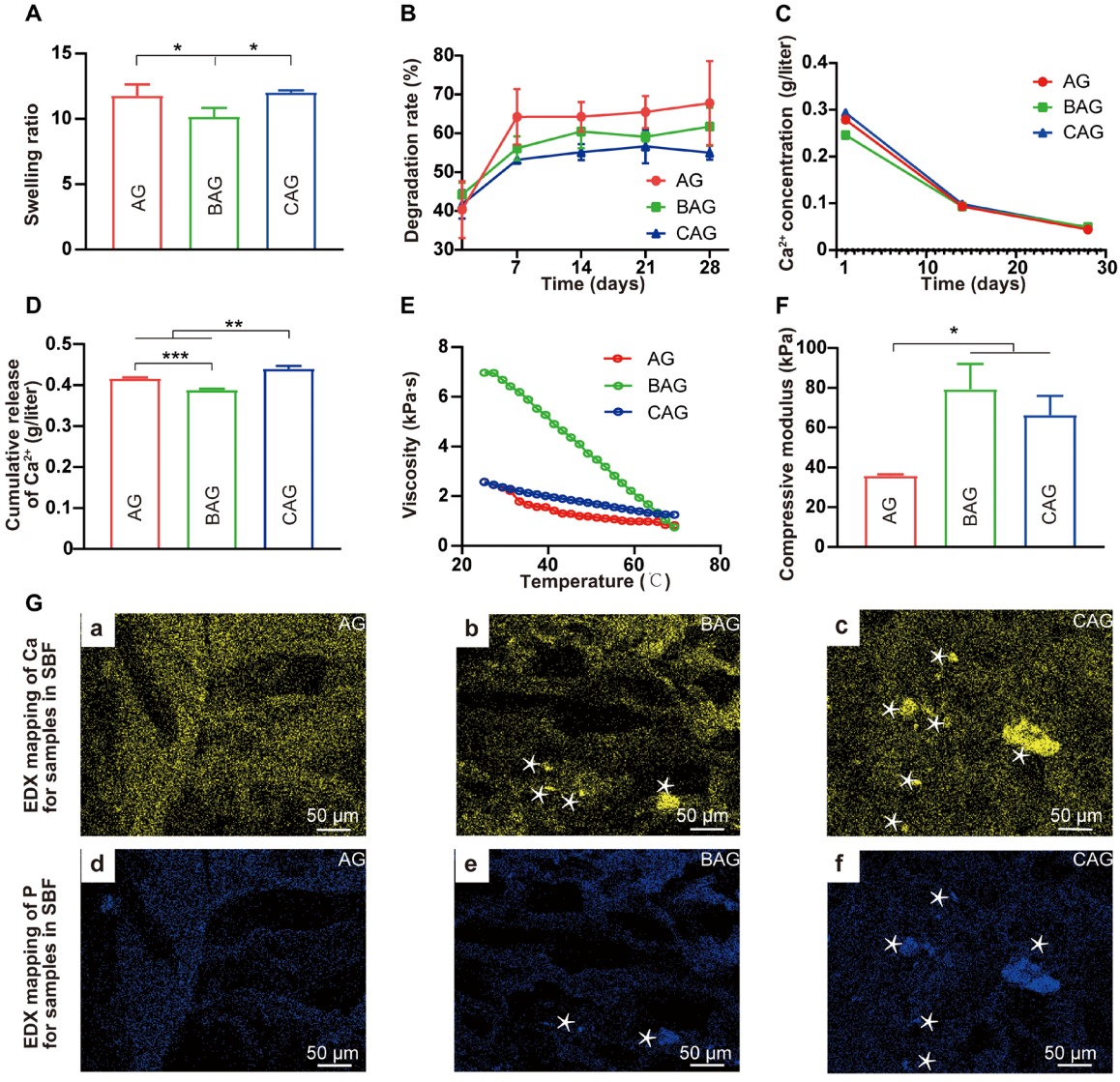

Fig. 4. Physiochemical properties and the apatite-forming ability of hydrogels. (**A**) Equilibrium swelling study of hydrogels. (**B**) Degradation test of hydrogels. (**C**) Concentration of Ca^{2+} released from hydrogels at 1, 14, and 28 days. (**D**) Cumulative release of Ca^{2+} from hydrogels for 28 days. $^{**}P < 0.01$, $^{***}P < 0.001$. (**E**) Viscosity versus temperature measurements of hydrogels. (**F**) Compressive modulus of hydrogels. * indicates statistically significant difference ($P < 0.05$) between groups. (**G**) Apatite-forming ability of hydrogels after immersing in simulated body fluid (SBF) for 28 days. Energy-dispersive x-ray spectroscopy (EDX) mapping of Ca in hydrogels (A to C). EDX mapping of P in hydrogels (D to F). The white asterisks in (G) (b, c, e, and f) exhibit distinct areas of Ca and P elements.

compared to BAG. Fluid retention leads to the relaxation of coiled polymer chains and an increase in CAG surface area, facilitating cellular infiltration into scaffolds (*32*). In addition, the enhanced swelling capacity of CAG allows for an efficient transport of nutrient between the extracellular matrix and the hydrogel (*32*). Once implanted in vivo, cells encapsulated in CAG are able to grow well in a nutrient-rich environment (*32*). However, the swollen state did not exist for a long time. Hydrogels degrade after implantation into the human body (*33*). Scaffolds are expected to degrade at a rate compatible with tissue regeneration (*33*). Herein, the degradation behavior of hydrogels was studied by detecting the change in gel weight over time. As shown in Fig. 4B, AG lost its weight fast in the first 7 days and reached a platform in the following 28 days. Incorporation of the inorganic component decreased the degradation rate of hydrogels. Notably, CAG exhibited a slower rate of weight loss compared to that of BAG. This phenomenon may be ascribed to the stable network of CAG generated by the electrostatic bonds between polymer matrices and inorganic particles (*34*). The stable degradation property allows CAG to maintain the osteogenic space for a long time after implanted into the human body which is beneficial for osteogenesis (*35*).

Following degradation, bioactive ions, such as calcium (Ca) and silicon (Si), were dissolved from hydrogels and may exert biological effects on surrounding cells (*36*). In the present study, the release pattern of Ca^{2+} was firstly detected by immersing hydrogels in the culture medium for 28 days. As shown in Fig. 4C, a burst release was observed at the first day for all groups, which was attributed to the sufficient ion exchange from hydrogel strands (*37*). The release

continued for longer than 4 weeks with a decreased rate. One reason for the slower release may be the formation of apatite layers on the BG (*38*). In addition, the degradative hydrogel absorbed much calcium to maintain the stability, reducing the calcium concentration in solution (*38*). A quantitative analysis of the cumulative release of Ca^{2+} from hydrogels was shown in Fig. 4D. The value of CAG group was significantly higher than that of other groups ($P < 0.05$). The highest amount of calcium released from CAG would substantially improve the microenvironment within the bone defect site and promote osteogenic differentiation of progenitor cells (*39*). The release pattern of Ca^{2+} is a dynamic process. It can be facilitated by the degradation of hydrogels and the dissolution of inorganic fillers (*40*), while it can also be consumed due to the formation of apatite layers on BG (*41*). The concentration of Ca^{2+} in pure BG solution could decrease first and then increase due to the deposition of calcium phosphate (*41*). CAG exhibited greater bioactivity than BAG as evidenced that semi-HA could already be observed during the preparation of CAG hydrogels (Fig. 2E). Therefore, when CAG was immersed in the medium for ion release, it was probably already in the stage of Ca ion increasing (*41*). As a comparison, calcium phosphate may have just started to deposit on BAG, which could consume some Ca ions. Taking all of the above into account, although the degradation rate of CAG is lower than that of BAG (Fig. 4B), the enhanced bioactivity of CAG may decrease the Ca consumption, leading to the higher Ca concentration in the medium (Fig. 4D). In addition, the release of Si ions from BAG and CAG for 14 days was shown in fig. S1. The enhanced release of Si from CAG compared with BAG was in accordance with a previous study (*42*). The hydrophilic property of amino groups on CAG may promote the Si release from hydrogels and further improve the osteogenic activity of hydrogels (*42*).

The mechanical properties of hydrogels were further investigated by rheology and compressive strength experiments. Figure 4E shows a graphical representation of the temperature-dependent viscosity change. For all samples, the viscosity of hydrogels decreased with increasing temperature owing to the thermotropic property of gellan gum in AG (*43*). CAG showed markedly decreased viscosity compared with that of BAG, which was probably due to the high surface-to-volume ratio of components in CAG (*21*). Such a low-viscosity polymer solution is considered to be suitable for manufacturing and practical applications (*44*). An optimal mechanical strength is equally necessary for bone regeneration applications. Hydrogels with suitable stiffness not only provide a static environment for tissue regeneration but also influence cellular response at the implantation site (*45*). In this study, the mechanical strength of different hydrogels was determined by a compression test (Fig. 4F). The result indicates that BAG and CAG exhibited increased compressive moduli relative to that of AG (79 ± 10 kPa and 66 ± 8 kPa, respectively). The strength was in the range of 40 to 100 kPa, which has been demonstrated to be beneficial for osteogenic differentiation of progenitor cells (*45*). However, the most favorable stiffness for the recruitment of stem cells in vivo has been demonstrated to be around 60 kPa in a rat segmental femoral defect model (*46*). Considering this, CAG in the present study is expected to show more pronounced osteogenic activity (*46*). Although the mechanical strength of hydrogels here is difficult to resist the external force at the load-bearing bone defect sites, these hydrogels can be used as bone defect fillers or coating agents for cancellous bone defects or low load-bearing bone defects (*8*). The mechanical strength changes of hydrogels should be further followed after implantation in vivo (*46*).

The apatite-forming ability of hydrogels

The apatite-forming ability of different hydrogels was investigated by immersing hydrogels in the simulated body fluid (SBF) for 28 days. As shown in fig. S2, white mineral particles precipitated on BAG and CAG, particularly on CAG. Precise elemental distribution of Ca and P was detected by SEM and energy-dispersive x-ray spectroscopy (EDX) mapping (Fig. 4G and fig. S2). Increased aggregation of Ca and P was observed on CAG compared with that on BAG, suggesting the enhanced HA biomineralization ability for CAG. A similar result was reported by Zhao *et al.* (*28*). The amino-modified BG exhibited superior apatite-forming activity compared with that of BG, which might be attributed to the strong electrostatic interaction between the initial nuclei of HA and amino groups on NBG (*28*).

Immune response of hydrogels in vitro

The immune response at the defect site should be carefully considered when developing a new type of bone substitute material (*47*). In this study, the cell migration ability and inflammatory gene expression were used to determine the immune response of RAW 264.7 after hydrogel treatment. Cell migration assay was first conducted to observe the interaction between immune cells and materials (*48*). The RAW 264.7 passing through the transwell chamber for 24 hours were observed and assessed by cell counting (Fig. 5, A, a to d, and B). BAG and CAG showed increased cell migration compared with that of control and AG, indicating a successful induction of immune response for BAG and CAG (*47*). The expression of M2-macrophage marker (CD206) was subsequently analyzed by flow cytometry to identify the macrophage phenotype (*49*). As shown in Fig. 5 (C and D), positive staining of the $CD206^+$ cells in CAG was significantly increased compared with that of other groups ($P < 0.05$; Fig. 5D). This strongly proves that CAG promoted macrophage polarization toward M2 phenotype more substantially than BAG or AG (*50*). Cytokine secretion was detected by quantitative reverse transcription polymerase chain reaction (qRT-PCR) to determine the inflammatory factor release of macrophages after hydrogel treatment (*51*). The expression of tumor necrosis factor–α (TNF-α), interleukin-1β (IL-1β), and IL-6 was decreased in CAG group compared with those in other groups ($P < 0.05$; Fig. 5, E to G), while the expression of anti-inflammatory cytokine, such as IL-10, was increased ($P < 0.05$; Fig. 5H). In this regard, CAG was considered to promote the M2 phenotype transition and a local anti-inflammatory microenvironment, probably by up-regulating the expression of IL-10 and down-regulating the expression of TNF-α, IL-1β, and IL-6 (*51*).

One reason for the different polarization may be attributed to the ion release from hydrogels (*52*). A previous study indicated that calcium concentration in the microenvironment notably affected the polarization stage of macrophages (*53*). The enhanced M2 polarization in CAG may have resulted from the increased calcium concentration surrounding the hydrogel (*53*). In addition, the suitable mechanical strength of CAG also probably had a positive effect on the M2 polarization of macrophages through improving the cytoskeleton architecture (*54*). After modulated to M2 phenotype, the macrophages in CAG could further recruit repairing cells to the implantation site, induce the anti-inflammatory stage, and activate the osteogenesis process (*55*).

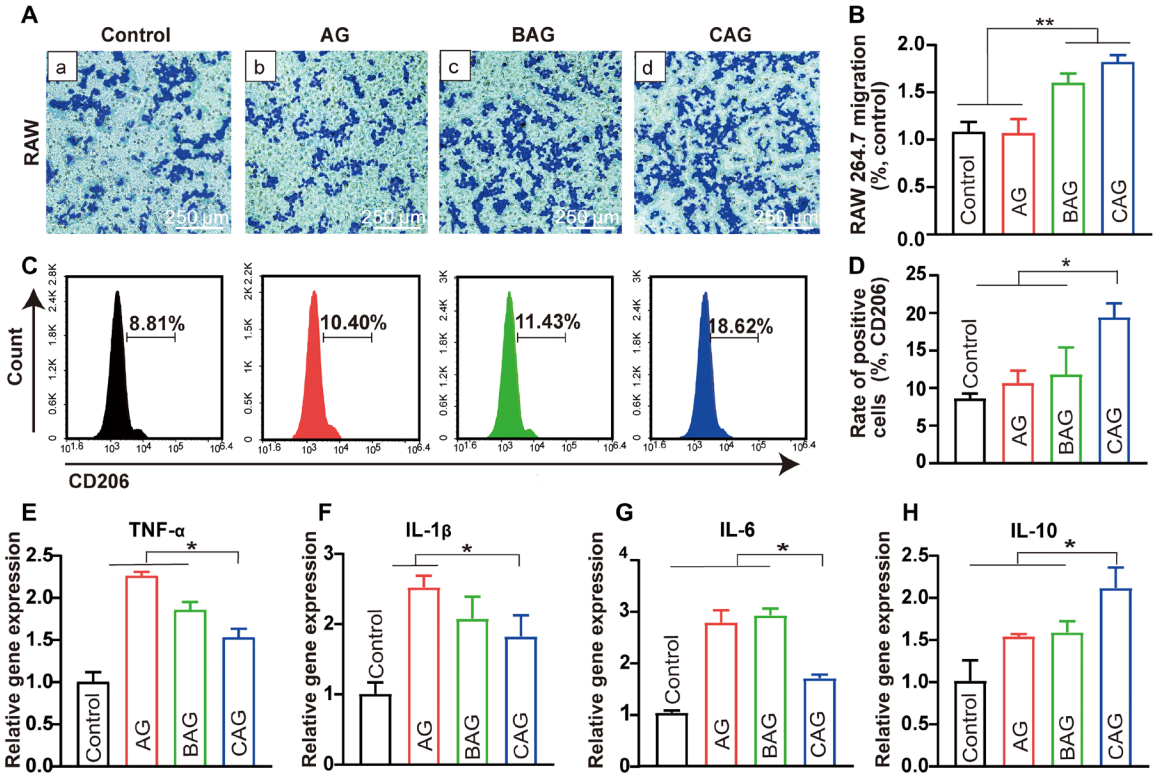

Fig. 5. Immune response of RAW 264.7 on hydrogels. (**A**) Migration of RAW 264.7 in the transwell assay. (a) Control, (b) AG, (c) BAG, and (d) CAG. (**B**) Number of migrated RAW 264.7 normalized to control group. $^{**}P < 0.01$. (**C**) Flow cytometry histogram of CD206 for RAW 264.7 cultured with different hydrogels. (**D**) Rate of positive cells for CD206 in RAW 264.7 cultured with different groups. (**E** to **H**) Inflammatory gene expression including tumor necrosis factor α (TNF-α), interleukin-1β (IL-1β), IL-6 and IL-10 of RAW 264.7 after cultured with hydrogels for 3 days. Note: TNF-α, IL-1β, IL-6, and IL-10. Gene expression of cells on tissue culture plates served as the calibrator. * indicates statistically significant difference ($P < 0.05$) between groups.

Osteogenic differentiation of cells on hydrogels

Cell biocompatibility is widely accepted to be an essential characteristic for biomaterials (*56*). Satisfied cell morphology and migration after hydrogel treatment are critically important for early tissue regeneration. In the present study, the cellular behavior of rat bone marrow stem cells (BMSCs) was evaluated to determine the biocompatibility of hydrogels. Figure 6A shows the cell morphology of BMSCs cultured on hydrogels for 24 hours. Cells cultured on the control, AG, and CAG exhibited favorable cell adhesion and spreading, while no noticeable cell pseudopodium was observed on BAG surface (Fig. 6A, a to d). The different cell morphologies indicate that the inorganic component significantly affected cell compatibility (*56*). CAG was beneficial for cell attachment and spreading, while BAG was not suitable for cell adhesion. Cell counting kit-8 (CCK-8) assay was used to investigate the effect of hydrogels on cell proliferation. As shown in Fig. 6B, the number of cells on hydrogels increased from 1 to 7 days ($P < 0.05$), while the values of different hydrogels were similar at each time point. In addition, BAG and CAG showed an increased migration of BMSCs compared to that of control and AG (Fig. 6C). In particular, CAG exhibited a higher recruitment effect than that of BAG ($P < 0.05$; Fig. 6D). The superior cell morphology and migration on CAG indicate that the electrostatically reinforced hydrogel has excellent biocompatibility (*48*). Both the optimal physical property and bioactivity of CAG contributed to the enhanced biocompatibility (*42*, *57*). First, the interfacial bond between organic and inorganic phases endowed CAG with a suitable porous structure, as demonstrated in the SEM analysis (*57*). Cell adhesion and migration were thus promoted in CAG taking advantage of the 3D porous structure (*57*). Second, the mechanical strength of CAG was sufficient to provide a suitable template for cell adhesion and migration as demonstrated in the mechanical test (*46*). Third, the inorganic NBG could exert a positive effect on cell biocompatibility (*42*). In a previous study, Zhang *et al.* (*42*) demonstrated that NBG with positive charges could accelerate cell adhesion and spreading by recruiting cells with a negatively charged membrane. The amino groups on NBG surface also behaved as anchor points for protein adsorption, which is beneficial for cell migration (*42*).

Alkaline phosphatase (ALP) is an early indicator of osteogenic differentiation (*6*). As shown in Fig. 6E, CAG exhibited a larger area of ALP staining than those of other groups at 7 days. Quantitative analysis of the ALP activity also showed that CAG had a higher value than that of other groups at both 3 and 7 days ($P < 0.05$; Fig. 6G). The enhanced ALP activity of CAG was due to its higher calcium release and suitable compressive strength (*58*, *59*). A previous study has indicated that an increase in Ca^{2+} could stimulate the chemotaxis and ALP activity of osteoblasts (*58*). In addition, the suitable compressive strength of CAG around 66 kPa may also be a critical factor leading to the increased ALP activity by modulating the expression of the extracellular matrix ligands on stem cells, such as integrin ligands (*59*).

Moreover, Alizarin red staining (ARS) was used to determine the mineralization at a late differentiation stage. The greatest mineral

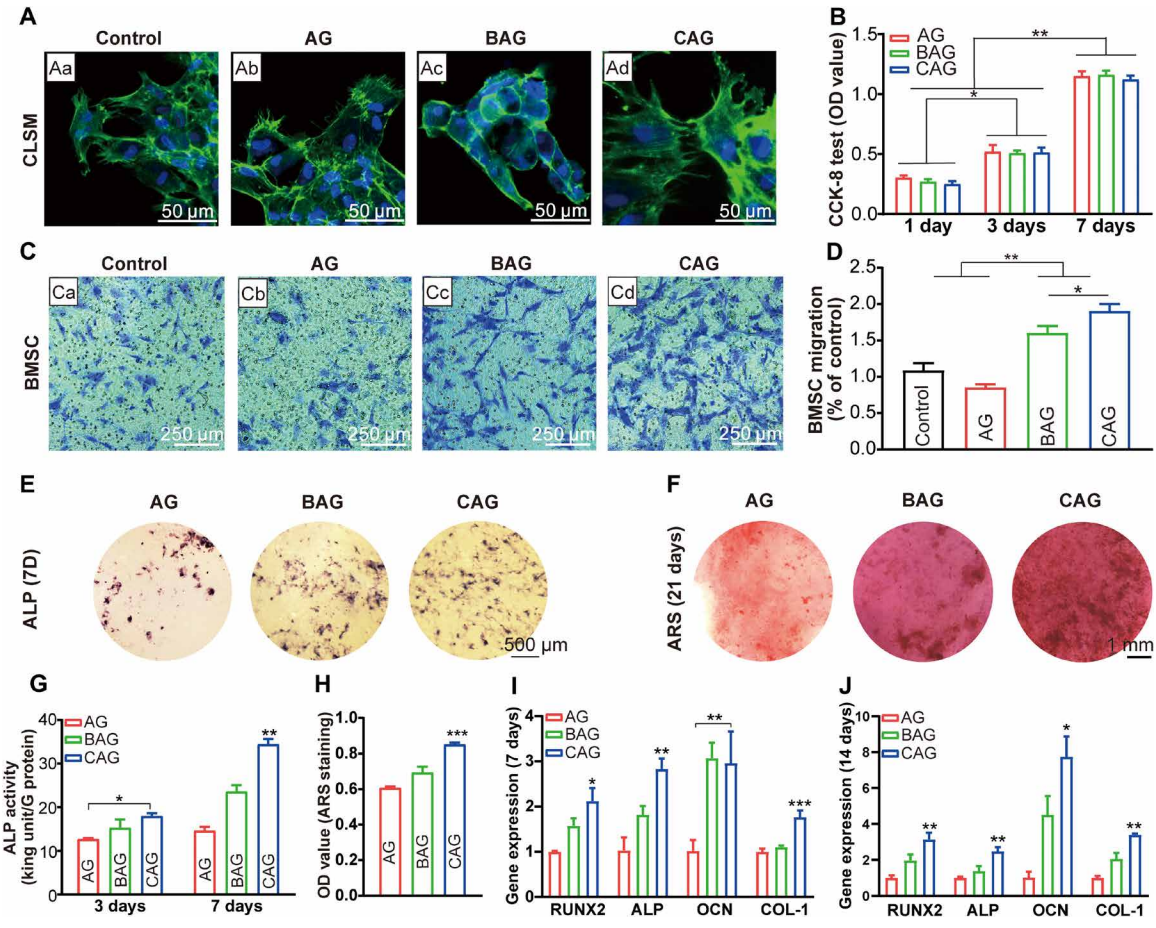

Fig. 6. Osteogenic differentiation of BMSCs cultured on hydrogels. (**A**) Confocal laser scanning microscopy (CLSM) images of cells cultured for 24 hours [(a), control, (b) AG, (c) BAG, and (d) CAG]. (**B**) Cell Counting kit-8 (CCK-8) assay of cells cultured for 1, 3, and 7 days. $^{**}P < 0.01$, $^{***}P < 0.001$. (**C**) Migration of BMSCs in the transwell assay. (Ca) Control, (Cb) AG, (Cc) BAG, and (Cd) CAG. (**D**) Number of migrated BMSCs normalized to control group. (**E**) Alkaline phosphatase (ALP) staining of cells cultured for 7 days. Images of (E) exhibit the same scale bar of 500 μm. (**F**) Alizarin red staining (ARS) of cells cultured for 21 days. Images of (F) exhibit the same scale bar of 1 mm. (**G**) ALP activity of cells cultured for 3 and 7 days. (**H**) Quantitative analysis of cell mineralization for 21 days. (**I** and **J**) Osteogenic gene expression of BMSCs cultured with different hydrogels for 7 days (I) and 14 days (J). Note: Runt-related transcription factor 2 (RUNX2), ALP activity, collagen type I (COL-1), and osteocalcin (OCN). Osteogenic gene expression of cells cultured on AG served as a calibrator. * indicates statistically significant difference ($P < 0.05$) between groups.

deposition was observed in CAG (Fig. 6, F and H), which is in accordance with the apatite-forming ability result, suggesting the enhanced osteogenesis of CAG (*6*). Gene expression test was subsequently conducted for runt-related transcription factor 2 (RUNX2), ALP, collagen-1 (COL-1), and osteocalcin (OCN) to determine the molecular effect of hydrogels on cell differentiation. As shown in Fig. 6 (I and J), the expression of RUNX2 and ALP was significantly higher for CAG compared with that of AG and BAG at 7 days ($P < 0.05$), confirming the increased osteogenesis of CAG at the early stage (*6*). The late marker of OCN showed nearly 7.7-fold increased expression for the CAG group on day 14. A similar expression pattern was also seen in a major extracellular matrix protein, COL-1. It was highly expressed in CAG at both 7 and 14 days ($P < 0.05$). The elevated gene expression of CAG may be resulted from the bioactivity of NBG. The amino groups on NBG surface have been demonstrated to absorb serum proteins and growth factors, which could further improve HA nucleation and direct anchorage of bone-forming cells and ultimately induce a long-term osteogenic signal pathway (*19*).

Bone formation ability of hydrogels in vivo

Given the enhanced osteogenic performance of CAG in vitro, a rat cranial defect model was further conducted to detect the bone regeneration ability of hydrogels in vivo. After hydrogel implantation, an inflammatory response was first induced within the body (*60*). A large number of macrophages were recruited to the defective region. M1 was the dominant phenotype within the first 24 hours, while a timely and smooth transition from M1 to M2 was necessary for the following bone regeneration (*60*). In the present study, the macrophage phenotype was determined by immunohistochemistry staining of inducible nitric oxide synthase (iNOS) and CD206 (*61*). As shown in Fig. 7A (e to h) and Fig. 7C, numerous $CD206^+$ (M2) cells were observed at the defect site of CAG group, while M1 remained the dominant phase in the samples treated with BAG with higher $iNOS^+$ expression [Fig. 7, A (a to d), and B]. The more noticeable staining of M2 marker in CAG has been confirmed to be of great importance in inducing an anti-inflammatory microenvironment and recruiting osteoprogenitor cells (*60*). The expression of BMSCs surface marker (CD44) was subsequently detected at the defect site

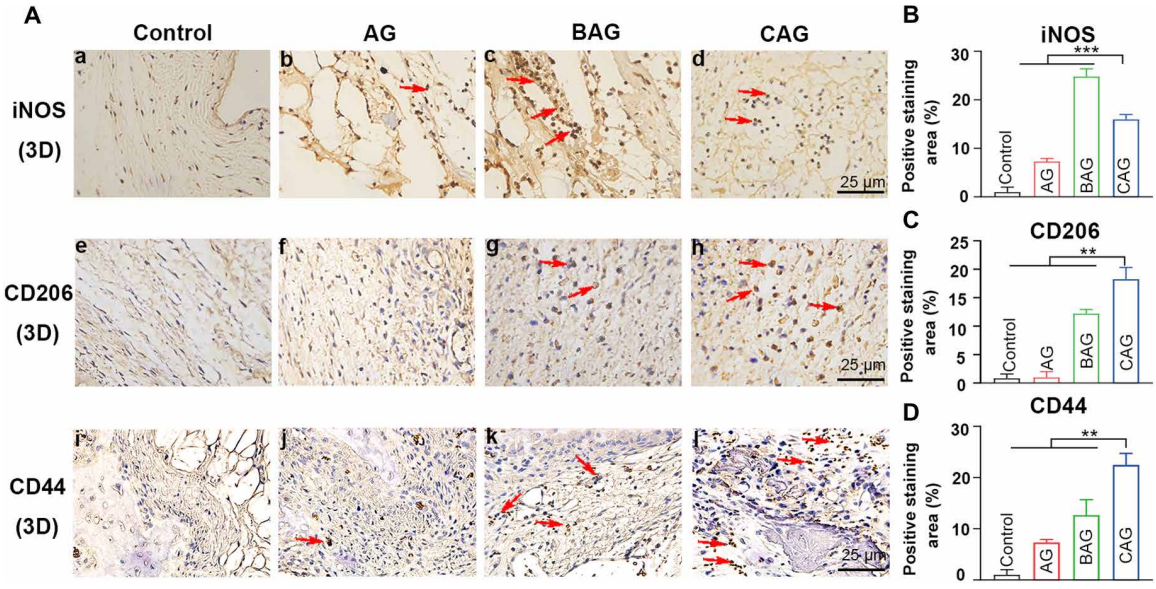

Fig. 7. Cell response at an early stage in a rat cranial defect model. (**A**, a to d) Immunohistochemistry staining of iNOS for macrophages. (A, e to h) Immunohistochemistry staining of CD206 for macrophages at the defect site. (A, i to l) Immunohistochemistry staining of CD44 for BMSCs. The red arrows indicate positively stained cells. Images of (A) (a to l) exhibit the same scale bar of 25 μm. (**B** to **D**) Quantitative analysis of positive stained area of inducible nitric oxide synthase (iNOS) (B), CD206 (C), and CD44 (D) for four groups. * indicates statistically significant difference ($P < 0.05$) between groups. **$P < 0.01$, ***$P < 0.001$.

by immunohistochemistry staining (Fig. 7A, i to l). The expression of CD44 was significantly increased in CAG group ($P < 0.01$; Fig. 7D), indicating the enhanced recruitment of BMSCs. This phenomenon is consistent with the previous in vitro results, as shown in Fig. 6C. The enhanced recruitment of BMSCs in vivo may be resulted from the morphological structure of CAG. As mentioned in the SEM result, the relatively larger pores of CAG facilitate the cell recruitment and bone ingrowth at the defect site, accelerating the process of bone repairing (*30*).

The bone regenerative efficacy was further detected by micro–computed tomography (μCT) and histological staining. Figure 8A shows μCT images of bone defects in the 2- and 8-week groups. Bone reconstruction of BAG and CAG was notably increased compared with that of control and AG at 8 weeks. In particular, the defect of CAG group was almost fully occupied by newly formed bone (Fig. 8A, h). The formation of new bone was quantitatively analyzed by calculating bone volume/tissue volume fraction (BV/TV), bone mineral density (BMD), trabecular thickness (Tb.Th), and structure model index (SMI), as shown in Fig. 8B. CAG exhibited the highest BV fraction compared to those of other groups ($P < 0.05$; Fig. 8B). A similar result was also found in the BMD analysis, in which the mean value of CAG group was two times higher than that of control group at 8 weeks. The increased BV/TV and BMD of CAG reflected a more compact structure of the newly formed bone which may greatly resist external forces (*62*). The strength of individual trabeculae was also determined by studying the average value of Tb.Th. There was no significant difference in Tb.Th among groups at 2 weeks, while the value of CAG at 8 weeks was higher than that of AG (Fig. 8B). In addition, the value of SMI represents an estimation of the plate-rod property of the bone structure. A higher value indicates a more rod-like trabeculae structure, while the lower value suggests a more plate-shaped trabeculae (*63*). The SMI of four groups was between 1 and 3, implying an identical plate-rod structure (*63*). While the lower value for CAG indicates a denser structure compared with that of other groups (*63*).

Sequential fluorescence labeling was used to compare the bone regeneration rate of different groups (*64*). As shown in Fig. 8C and fig. S3A, defect sites with hydrogel treatment showed markedly higher mineral deposition compared with the control group. In particular, CAG exhibited the highest bone regeneration rate at all predetermined time points (*64*). Then, hematoxylin and eosin (H&E) and Masson trichrome staining were applied to determine the quality of newly formed bone in detail at 8 weeks (Fig. 8D). The control group showed only a small quantity of newly formed bone at the defect margin (Fig. 8 D, a and b). For the hydrogel groups, undegraded materials still remained at the defect site and new bone formation (black arrows) was mainly presented at the center of hydrogels. The area of mineralized bone in BAG was higher than that of AG, indicating the enhanced osteoinductivity of BG (*65*). However, more mature bone originated from the margin of defects in CAG (except for the osteoid bone), confirming the enhanced cell recruitment ability of BMSCs on CAG (*66*). The quantitative analysis of new bone formation also indicates that CAG exhibited enhanced bone regeneration ability (fig. S3B) (*64*). Several factors participated in the healing process to promote bone regeneration of CAG (*28*, *46*). The Ca-P–rich layer on the hydrogel surface was critical for the formation of a direct bond between bone and hydrogels (*28*). The higher apatite-forming ability of CAG promoted HA growth and bone formation (*28*). In addition, a hydrogel with a stiffness of 60 kPa was confirmed to notably increase the BMD of newly formed bone and regenerate the skull defects in immunocompromised nude rats (*46*). The matched stiffness of CAG in the present study may be another important factor leading to the enhanced bone regeneration in vivo (*46*).

In summary, our results have shown that improving interfacial compatibility between different phases in composites simply by

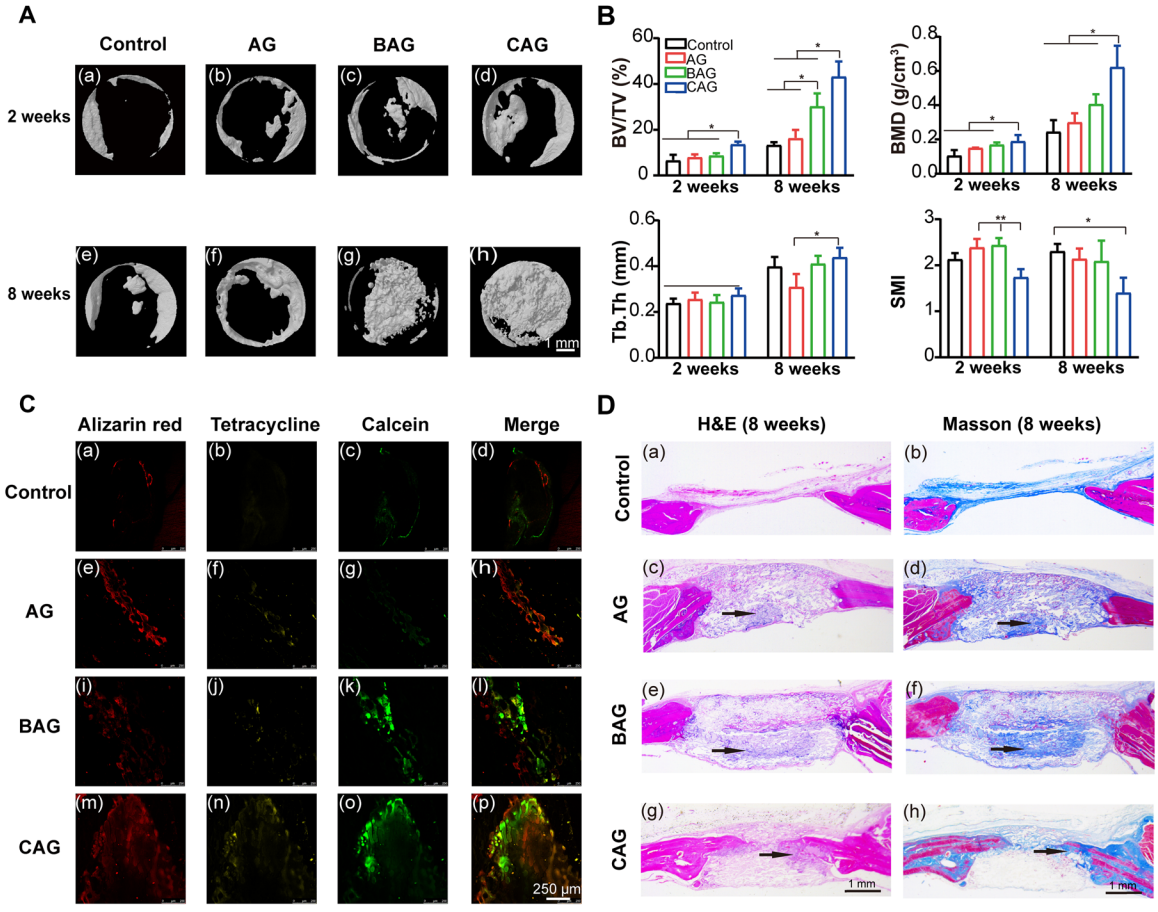

Fig. 8. Newly bone formation in a rat cranial bone defect model. (**A**) μCT images of calvaria samples, (A, a to d) samples from 2-week post-surgery group. (A, e to h) Samples from 8-week post-surgery group. Images of (A) (a to h) exhibit the same scale bar of 1 mm. (**B**) Quantitative analysis of newly bone formation at 2 and 8 weeks. Notes: Bone volume/tissue volume (BV/TV), bone marrow density (BMD), trabecular thickness (Tb.Th), and structure model index (SMI). *$P < 0.05$, **$P < 0.01$. (**C**) Representative sequential fluorescent staining for alizarin red, tetracycline, and calcein at 1, 3, and 5 weeks. (C, a to p) Images share the same scale bar of 250 μm. (**D**) H&E and Masson's trichrome staining of samples at 8 weeks, H&E staining was shown in (D) (a, c, e, and g) and Masson's trichrome staining in (D) (b, d, f, and h). Images of (D) (a to h) exhibit the same scale bar of 1 mm. Black arrows in the figure suggest the mineralized zone.

introducing the functionalized BG, rather than developing a new, complex inorganic phase can also enhance biological properties of composite hydrogels toward improved bone regeneration, which provides a convenient approach to develop novel composite hydrogels that can be translated to clinical applications (*10*).

METHODS

Materials

The BG in this study was commercially obtained from Aladdin (Shanghai, China). It was fabricated using a conventional melt-quenching method with a composition of 45% SiO_2, 24.5% CaO, 24.5% Na_2O, and 6% P_2O_5 (in wt %), and the size of particles was in a range of 10 to 100 μm. AG were both bought from Sigma-Aldrich (St. Louis, MO, USA).

Surface functionalization of bioactive glass

The amino-functionalized BG (NBG) was obtained via a post-synthesis procedure using (3-aminopropyl) trimethoxysilane (APTMS; Aladdin, China). BG (0.5 g) was dispersed in 250 ml of a 95 volume % ethanol solution (Aladdin, China), which was supplemented with 5 ml of APTMS (400 rpm, 24 hours, 50°C). The amino-modified BG (NBG) with a cationic surface was lastly obtained by centrifuging at 5000 rpm for 5 min and drying at 60°C overnight (*29*).

Fabrication of hydrogels

AG was prepared according to a previous study (*17*). Briefly, alginate [3% (w/v)] and gellan gum [3.5% (w/v)] powders were dissolved in a 0.03% (w/v) $CaCl_2$ solution (Aladdin, China) followed by magnetic stirring at 90°C and 300 rpm for 1 hour (*67*). The solution was cooled to room temperature and further placed in 1 M $CaCl_2$ for 10 min to enhance hydrogel cross-linking. The matrices containing BG and NBG at a concentration of 1% (w/v) were prepared according to the same method described above. The incorporation ratio of inorganic particles was determined by a CCK-8 and ALP test based on a previous study (*24*). The hydrogel with a BG mixing ratio of 1% (w/v) showed a higher biocompatibility (*24*). The method and figure were shown in the Supplementary Materials (fig. S4). AG, BAG, and CAG denote the pure hydrogel and hydrogels including BG and NBG, respectively.

Structural analysis

XPS (Thermo VG Scientific, USA) was first used to detect the amino groups presented on NBG surface. Zeta potential analyzer (Brookhaven Corporate Park, Holtsville, USA) was used to detect the interfacial interaction in hydrogels. FTIR (Thermo Fisher Scientific) analysis was further applied to detect the possible functional groups presented in hydrogels. XRD (D8 Focus, Bruker) was used to determine the crystallinity of hydrogels by Cu Ka radiation in a 2θ range of 10° to 80°. The different morphology of BG and NBG was investigated by SEM (S-3400 N, Hitachi, Japan) analysis. The cross-sectional morphology of hydrogels was also observed using SEM. Samples were lyophilized and mounted onto copper studs before observation.

Equilibrium swelling and degradation test

The equilibrium swelling ratio was used to evaluate the substance exchange function of hydrogels (*6*). Lyophilized hydrogels were first weighed. Swollen hydrogels were obtained by immersing them in 3 ml of phosphate-buffered solution (PBS; pH = 7.4), which were then weighted. The final swelling ratio of hydrogels was calculated using the following formula

$$\text{Swelling ratio} = (Ws - Wd)/Wd \quad (1)$$

where *W*d and *W*s represent the weight of lyophilized and swollen gels, respectively.

For the degradation test, dried samples were prepared, weighed, and immersed in 3 ml of PBS. After 3, 7, 14, 21, and 28 days, the remaining hydrogels were lyophilized and weighed. The degradation rate was calculated using the following equation

$$\text{Degradation rate (\%)} = (Wd - Wt)/Wd \times 100 \quad (2)$$

where *W*d and *W*t represent the weight of initial and remaining dried gels at time *t*, respectively.

Ca^{2+} release in the cell culture medium

To identify the amount of calcium released from hydrogels in vitro, samples (500 μl) were immersed in 5 ml of cell culture medium at 37°C. After 1, 14, and 28 days, the medium was collected and transferred to new tubes. The calcium concentration in the medium was determined using inductively coupled plasma atomic emission spectrometry (iCAP6300, Thermo Fisher Scientific, USA).

Rheological measurement and mechanical test

A rheometer (TA Instruments Co., AR 2000ex) was used to investigate the rheological behavior of different hydrogel solution. The effect of temperature on gel viscosity was evaluated at a frequency of 1 Hz and 1% strain. After gelation, the mechanical strength of swollen hydrogels (13 mm in diameter and 6 mm in thickness) was investigated by a dynamic mechanical analyzer (DMA 8000, PerkinElmer, USA) at room temperature. The compressive modulus was calculated from a linear fit of the stress-strain curve between strains of 10 and 20%.

Apatite-forming ability of hydrogels

Disc-shaped specimens with 8 mm in width and 2 mm in height were prepared using silicon molds for the apatite-forming test. After immersing in the 3 ml of SBF solution (COOLABER, China) at 37°C for 28 days, the apatite-like layer formed on the hydrogel surface was observed and analyzed by SEM. The elemental distribution of Ca and P on the cross-sectional surface was determined by EDX using a system attached to S-3400N SEM.

Cell culture

Cells used in the present study included BMSCs (passages 3 to 5) and murine macrophage cell line RAW 264.7. The cells were cultured in Dulbecco's modified Eagle's medium (DMEM; Hyclone, USA) supplemented with 10% heat-inactivated fetal bovine serum (Hyclone, USA) at 37°C in a humidified CO_2 incubator. Hydrogels were prepared with punches and sterilized by ultraviolet light for 1 hour before use.

Immune response of RAW 264.7 on hydrogels

The cell migration ability after hydrogel treatment was investigated by a transwell assay. Briefly, hydrogels (1 cm in diameter and 1 mm in depth) were placed in the lower transwell chamber (Costar, Corning, USA), and RAW 264.7 cells (1×10^4 cells/ml) were seeded onto the upper chamber. After 24 hours of incubation, cells passing through the transwell membrane were stained with 0.1% (w/v) crystal violet (Sigma-Aldrich). The migrated cells were observed using an optical microscope (Nikon, Japan) and calculated by ImageJ software (National Institutes of Health, Bethesda). Flow cytometry was used to investigate the phenotype of recruited macrophages after hydrogels treatment. Briefly, RAW 264.7 cells were seeded at 5×10^5 cells per well in 24-well culture plates. After 24 hours, cells were treated with different hydrogel extract or fresh medium for 3 days. The ratio of cells with M2 phenotype was detected by determining the expression of CD206 on the macrophage surface using flow cytometry (NovoCyte, Agilent). The antibodies used in this analysis were Alexa Fluor 647 Rat Anti-Mouse CD206 (BD Pharmingen, USA) and its isotype control (BD Pharmingen, USA). qRT-PCR was further used to detect the expression of inflammatory-related genes after hydrogel treatment. Total RNA was extracted from cells and reverse-transcribed to cDNA using the PrimeScript RT Reagent Kit (TaKaRa, Japan). qRT-PCR was carried out using the TB Green Kit (TaKaRa, Japan) on a Light cycler 480 system (Roche, Mannheim, Germany). The gene expression level was calculated using the $2^{-\Delta\Delta Ct}$ method for the following genes: TNF-α, IL-1β, IL-6, and IL-10. The sequences of primers are listed in table S1.

Cell adhesion and proliferation of BMSCs on hydrogels

The cell morphology of BMSCs cultured on different hydrogels was determined by cytoskeleton staining. Briefly, cells were seeded on the hydrogels at a density of 2×10^4 cells per gel in a 48-well tissue plate. After 24 hours, cells were fixed and incubated with fluorescein isothiocyanate–phalloidin (100 μg ml^{-1}; Sigma-Aldrich, USA) for 40 min and 4′,6-diamidino-2-phenylindole (10 μg ml^{-1}; Sigma-Aldrich, USA) for 5 min. The cell morphology was then observed using a confocal laser scanning microscope (CLSM; LSM880, Zeiss, Germany). Cell viability was further detected using a CCK-8 kit (Beyotime, China). A seeding density of 5000 cells per well in a 96-well tissue plate was used. After 1, 3, and 7 days, CCK-8 solution was added to the culture plate and further incubated for 1 hour at 37°C. The optical density (OD) of the mixture was measured using a Synergy HT spectrophotometer (BioTek Instruments). The migration ability of BMSCs was also detected by a transwell assay. The procedure has been mentioned in the section above.

ALP activity of BMSCs on hydrogels

ALP expression was used to detect the osteogenic differentiation at an early stage (*6*). The experiment was conducted following the protocol of an ALP kit (Jiancheng Institute of Bioengineering, Nanjing, China). Briefly, BMSCs were seeded at a density of 10^5 cells/ml on the hydrogels. After incubation for 3 and 7 days, cells were lysed and reacted with chromogenic agents. The OD value at 405 nm was recorded and further calculated using a formula in the kit. The final ALP activity was normalized to the protein concentration measured using a BCA kit (Beyotime, Shanghai, China). For direct observation of ALP expression, ALP staining of cells cultured on hydrogels for 7 days was evaluated using a bromochloroindolyl phosphate–nitro blue tetrazolium kit (Beyotime, Shanghai). The area and darkness of staining were observed using an optical microscope.

Cell mineralization of BMSCs on hydrogels

ARS was used to determine cell mineralization at the late differentiation stage (*6*). After an incubation of 21 days, cells on the hydrogels were fixed and stained using ARS kit (Sigma-Aldrich). The mineralized nodules were observed using a microscope. Further quantitative analysis was conducted by eluting the deposit with 10% cetylpyridinium chloride (Sigma-Aldrich). The OD value of the eluted solution was measured at 550 nm, and the result of AG group was used for calibration.

Osteogenic gene expression of BMSCs on hydrogels

RUNX2 and ALP are typical osteogenic genes expressed in the early stage, while COL-1 and OCN are typically detected in the late stage. In the present study, the osteogenic performance of hydrogels at a gene level was evaluated by detecting the expression of RUNX2, ALP, COL-1, and OCN. β-Actin served as a house-keeping gene control. The experiment was conducted as mentioned above and the primer sequences are shown in table S2.

Surgical procedure of animal studies in vivo

Bone formation in vivo after hydrogel treatment was detected using a rat calvarial bone defect model. Forty-eight Sprague-Dawley rats (200 to 250 g, 8 weeks, male) were used in the present study and divided into four groups (control, AG, BAG, and CAG). The control group had cranial defects with no materials. After anesthesia, the rat cranium was shaved and disinfected. An incision of approximately 2 cm was made along the sagittal suture of the calvarium. The subcutaneous tissue was bluntly dissected. Bone defects with a diameter of 5 mm were subsequently created on both sides of the parietal bone using a trephine drilling. Hydrogels with a diameter of 5 mm and depth of 1 mm were inserted into the bone defects. The skin incision was closed using 4-0 silk sutures. At 3 days, 2 weeks, and 8 weeks after surgery, animals were euthanized. Calvarium samples were collected and fixed with formalin for 48 hours. The experiment was approved by the Animal Care and Use Committee of the Ninth People's Hospital affiliated to Shanghai Jiaotong University, School of Medicine.

μCT scanning

μCT analysis of specimens from 2- and 8-week groups was performed using a μCT (SkyScan 1076, Belgium). The scanning voltage and electric current were 40 kV and 250 μA, respectively. The new bone formation was observed by 3D images of calvariums using SkyScan software. Further quantitative analysis of the new bone formation was determined by BV/TV, BMD, Tb.Th, and SMI at the defect site.

Sequential fluorescent labeling

A time course of bone formation was evaluated by polychrome fluorescent labeling in 12 rats from the 8-week group. At 1, 3, and 5 weeks after operation, fluorochromes were administered intraperitoneally in the following order: Alizarin red (30 mg/kg; Sigma-Aldrich), tetracycline (25 mg/kg; Sigma-Aldrich), and calcein (20 mg/kg; Sigma-Aldrich). At 8 weeks after surgery, samples were harvested and prepared for hard tissue sectioning following a previous study (*64*). Dynamic bone formation was evaluated by observing and calculating the area stained by fluorescence labels using CLSM.

Histological staining and immunohistochemistry staining

Histological regeneration of bone defects after hydrogel treatment was investigated by H&E and Masson's trichrome staining. Calvariums in the 8-week group expect those for fluorescent labeling, were decalcified for 1 month, and embedded in paraffin. Sample sections were obtained by cutting bone defects following the coronal plane and then stained with H&E and Masson's trichrome stains. Calvariums from 3-day group were used to detect the expression of M1-macrophage marker (iNOS), M2-macrophage marker (CD206), and cell surface marker of BMSCs (CD44) at the defect site by immunohistochemistry staining. The sections were prepared as described for histological staining. Primary antibody against iNOS (Abcam, UK), CD206 (Abcam, UK), and CD44 (R&D Systems, USA) was used to detect the expression of iNOS, CD206, and CD44, respectively, following the kit protocol. The area of $iNOS^+$, $CD206^+$, and $CD44^+$ regions were observed with an optical microscope and quantitatively analyzed using ImageJ.

Statistical analysis

All measurements are represented as the means ± SD. The difference between groups was analyzed by one-way analysis of variance (ANOVA) and Tukey's post hoc test. The statistical analysis was conducted using GraphPad Prism software (GraphPad Software Inc., USA). The result of $^*P < 0.05$ was considered to be statistically different.

SUPPLEMENTARY MATERIALS

Supplementary material for this article is available at https://science.org/doi/10.1126/sciadv.abj7857

View/request a protocol for this paper from *Bio-protocol*.

REFERENCES AND NOTES

1. Y. Yang, L. Chu, S. Yang, H. Zhang, L. Qin, O. Guillaume, D. Eglin, R. G. Richards, T. Tang, Dual-functional 3D-printed composite scaffold for inhibiting bacterial infection and promoting bone regeneration in infected bone defect models. *Acta Biomater.* **79**, 265–275 (2018).
2. H. J. Haugen, S. P. Lyngstadaas, F. Rossi, G. Perale, Bone grafts: Which is the ideal biomaterial? *J. Clin. Periodontol.* **46**, 92–102 (2019).
3. Z. Shi, X. Gao, M. W. Ullah, S. Li, Q. Wang, G. Yang, Electroconductive natural polymer-based hydrogels. *Biomaterials* **111**, 40–54 (2016).
4. J. Kapr, L. Petersilie, T. Distler, I. Lauria, F. Bendt, C. M. Sauter, A. R. Boccaccini, C. R. Rose, E. Fritsche, Human induced pluripotent stem cell-derived neural progenitor cells produce distinct neural 3D in vitro models depending on alginate/gellan gum/laminin hydrogel blend properties. *Adv. Healthc. Mater.* **10**, 2100131 (2021).
5. A. Akkineni, T. Ahlfeld, A. Funk, A. Waske, A. Lode, M. Gelinsky, Highly concentrated alginate-gellan gum composites for 3D plotting of complex tissue engineering scaffolds. *Polymers* **8**, 170 (2016).

6. X. Ding, X. Li, C. Li, M. Qi, Z. Zhang, X. Sun, L. Wang, Y. Zhou, Chitosan/dextran hydrogel constructs containing strontium-doped hydroxyapatite with enhanced osteogenic potential in rat cranium. *ACS Biomater. Sci. Eng.* **5**, 4574–4586 (2019).
7. A. Kumar, S. S. Han, Enhanced mechanical, biomineralization, and cellular response of nanocomposite hydrogels by bioactive glass and halloysite nanotubes for bone tissue regeneration. *Mater. Sci. Eng. C* **128**, 112236 (2021).
8. J. A. Killion, S. Kehoe, L. M. Geever, D. M. Devine, E. Sheehan, D. Boyd, C. L. Higginbotham, Hydrogel/bioactive glass composites for bone regeneration applications: Synthesis and characterisation. *Mater. Sci. Eng. C* **33**, 4203–4212 (2013).
9. J. Faure, R. Drevet, A. Lemelle, N. Ben Jaber, A. Tara, H. El Btaouri, H. Benhayoune, A new sol–gel synthesis of 45S5 bioactive glass using an organic acid as catalyst. *Mater. Sci. Eng. C* **47**, 407–412 (2015).
10. A. K. Miri, N. Muja, N. O. Kamranpour, W. C. Lepry, A. R. Boccaccini, S. A. Clarke, S. N. Nazhat, Ectopic bone formation in rapidly fabricated acellular injectable dense collagen-Bioglass hybrid scaffolds via gel aspiration-ejection. *Biomaterials* **85**, 128–141 (2016).
11. T. Montheil, C. Cile Echalier, J. Martinez, G. Subra, A. Mehdi, Inorganic polymerization: An attractive route to biocompatible hybrid hydrogels. *J. Mater. Chem. B* **6**, 3434–3448 (2018).
12. U. Rottensteiner, B. Sarker, D. Heusinger, D. Dafinova, S. N. Rath, J. P. Beier, U. Kneser, R. E. Horch, R. Detsch, A. R. Boccaccini, A. Arkudas, In vitro and in vivo biocompatibility of alginate dialdehyde/gelatin hydrogels with and without nanoscaled bioactive glass for bone tissue engineering applications. *Materials* **7**, 1957–1974 (2014).
13. O. Sánchez-Aguinagalde, A. Lejardi, E. Meaurio, R. Hernández, C. Mijangos, J. R. Sarasua, Novel hydrogels of chitosan and poly (Vinyl alcohol) reinforced with inorganic particles of bioactive glass. *Polymers* **13**, 691 (2021).
14. H. Hosseinzadeh, K. Abdi, Efficient removal of methylene blue using a hybrid organic-inorganic hydrogel nanocomposite adsorbent based on sodium alginate-silicone dioxide. *J. Inorg. Organomet. Polym. Mater.* **27**, 1595–1612 (2017).
15. Q. Gao, C. Zhang, M. Wang, Y. Wu, C. Gao, P. Zhu, Injectable pH-responsive poly (γ-glutamic acid)-silica hybrid hydrogels with high mechanical strength, conductivity and cytocompatibility for biomedical applications. *Polymer* **197**, 122489 (2020), 122489.
16. J. R. Jones, Reprint of: Review of bioactive glass: From Hench to hybrids. *Acta Biomater.* **23**, S53–S82 (2015).
17. M. Lee, K. Bae, P. Guillon, J. Chang, Ø. Arlov, M. Zenobi-Wong, Exploitation of cationic silica nanoparticles for bioprinting of large-scale constructs with high printing fidelity. *ACS Appl. Mater. Interfaces* **10**, 37820–37828 (2018).
18. H. H. Lu, S. R. Pollack, P. Ducheyne, 45S5 Bioactive glass surface charge variations and the formation of a surface calcium phosphate layer in a solution containing fibronectin. *J. Biomed. Mater. Res.* **54**, 454–461 (2001).
19. X. Zhang, D. Zeng, N. Li, J. Wen, X. Jiang, C. Liu, Y. Li, Functionalized mesoporous bioactive glass scaffolds for enhanced bone tissue regeneration. *Sci. Rep.* **6**, 19361 (2016).
20. S. Basu, S. Pacelli, Y. Feng, Q. Lu, J. Wang, A. Paul, Harnessing the noncovalent interactions of DNA backbone with 2D silicate nanodisks to fabricate injectable therapeutic hydrogels. *ACS Nano* **12**, 9866–9880 (2018).
21. J. R. Xavier, T. Thakur, P. Desai, M. K. Jaiswal, N. Sears, E. Cosgriff-Hernandez, R. Kaunas, A. K. Gaharwar, Bioactive nanoengineered hydrogels for bone tissue engineering: A growth-factor-free approach. *ACS Nano* **9**, 3109–3118 (2015).
22. H. Y. Lee, S. H. Park, J. H. Kim, M. S. Kim, Temperature-responsive hydrogels via the electrostatic interaction of amphiphilic diblock copolymers with pendant-ion groups. *Polym. Chem.* **8**, 6606–6616 (2017).
23. W. Wang, Y. Zhao, H. Bai, T. Zhang, V. Ibarra-Galvan, S. Song, Methylene blue removal from water using the hydrogel beads of poly(vinyl alcohol)-sodium alginate-chitosan-montmorillonite. *Carbohydr. Polym.* **198**, 518–528 (2018).
24. B. Sarker, W. Li, K. Zheng, R. Detsch, A. R. Boccaccini, Designing porous bone tissue engineering scaffolds with enhanced mechanical properties from composite hydrogels composed of modified alginate, gelatin, and bioactive glass. *ACS Biomater. Sci. Eng.* **2**, 2240–2254 (2016).
25. Y. Luo, A. Lode, C. Wu, J. Chang, M. Gelinsky, Alginate/nanohydroxyapatite scaffolds with designed core/shell structures fabricated by 3D plotting and in situ mineralization for bone tissue engineering. *ACS Appl. Mater. Interfaces* **7**, 6541–6549 (2015).
26. K. Zheng, X. Dai, M. Lu, N. Hüser, N. Taccardi, A. R. Boccaccini, Synthesis of copper-containing bioactive glass nanoparticles using a modified Stöber method for biomedical applications. *Colloids Surf. B Biointerfaces* **150**, 159–167 (2017).
27. M. Valero, B. Zornoza, C. Téllez, J. Coronas, Mixed matrix membranes for gas separation by combination of silica MCM-41 and MOF NH2-MIL-53(Al) in glassy polymers. *Microporous Mesoporous Mater.* **192**, 23–28 (2014).
28. S. Zhao, J. Zhang, M. Zhu, Y. Zhang, Z. Liu, Y. Ma, Y. Zhu, C. Zhang, Effects of functional groups on the structure, physicochemical and biological properties of mesoporous bioactive glass scaffolds. *J. Mater. Chem. B* **3**, 1612–1623 (2015).
29. A. El-Fiqi, T.-H. Kim, M. Kim, M. Eltohamy, J.-E. Won, E.-J. Lee, H.-W. Kim, Capacity of mesoporous bioactive glass nanoparticles to deliver therapeutic molecules. *Nanoscale* **4**, 7475–7488 (2012).
30. V. Karageorgiou, D. Kaplan, Porosity of 3D biomaterial scaffolds and osteogenesis. *Biomaterials* **26**, 5474–5491 (2005).
31. S. Zhao, Z. Wang, H. Kang, W. Zhang, J. Li, S. Zhang, L. Li, A. Huang, Construction of bioinspired organic-inorganic hybrid composite by cellulose-induced interfacial gelation assisted with Pickering emulsion template. *Chem. Eng. J.* **359**, 275–284 (2019).
32. S. Dhivya, S. Saravanan, T. P. Sastry, N. Selvamurugan, Nanohydroxyapatite-reinforced chitosan composite hydrogel for bone tissue repair in vitro and in vivo. *J. Nanobiotechnology* **13**, 40 (2015).
33. G. Camci-Unal, D. Cuttica, N. Annabi, D. Demarchi, A. Khademhosseini, Synthesis and characterization of hybrid hyaluronic acid-gelatin hydrogels. *Biomacromolecules* **14**, 1085–1092 (2013).
34. A. Nguyen-My Le, T. T. Nguyen, K. L. Ly, T. D. Luong, M. H. Ho, N. Minh-Phuong Tran, N. Ngoc-Thao Dang, T. Van Vo, Q. N. Tran, T. H. Nguyen, Modulating biodegradation and biocompatibility of in situ crosslinked hydrogel by the integration of alginate into N,O-carboxylmethyl chitosan – aldehyde hyaluronic acid network. *Polym. Degrad. Stab.* **180**, 109270 (2020).
35. L.-B. Jiang, D.-H. Su, S.-L. Ding, Q.-C. Zhang, Z.-F. Li, F.-C. Chen, W. Ding, S.-T. Zhang, J. Dong, Salt-assisted toughening of protein hydrogel with controlled degradation for bone regeneration. *Adv. Funct. Mater.* **29**, 1901314 (2019).
36. J. Wu, K. Zheng, X. Huang, J. Liu, H. Liu, A. R. Boccaccini, Y. Wan, X. Guo, Z. Shao, Thermally triggered injectable chitosan/silk fibroin/bioactive glass nanoparticle hydrogels for in-situ bone formation in rat calvarial bone defects. *Acta Biomater.* **91**, 60–71 (2019).
37. G. Luo, Y. Ma, X. Cui, L. Jiang, M. Wu, Y. Hu, Y. Luo, H. Pan, C. Ruan, 13-93 bioactive glass/alginate composite scaffolds 3D printed under mild conditions for bone regeneration. *RSC Adv.* **7**, 11880–11889 (2017).
38. V. Guduric, N. Belton, R. F. Richter, A. Bernhardt, J. Spangenberg, C. Wu, A. Lode, M. Gelinsky, Tailorable zinc-substituted mesoporous bioactive glass/alginate-methylcellulose composite bioinks. *Materials* **14**, 1225 (2021).
39. A. El-Fiqi, J.-H. Kim, H.-W. Kim, Osteoinductive fibrous scaffolds of biopolymer/mesoporous bioactive glass nanocarriers with excellent bioactivity and long-term delivery of osteogenic drug. *ACS Appl. Mater. Interfaces* **7**, 1140–1152 (2015).
40. A. Haider, A. Waseem, N. Karpukhina, S. Mohsin, Strontium-and zinc-containing bioactive glass and alginates scaffolds. *Bioengineering* **7**, 10 (2020).
41. K. Zheng, N. Taccardi, A. M. Beltrán, B. Beltrán, B. Sui, T. Zhou, V. R. Reddy Marthala, M. Hartmann, A. R. Boccaccini, Timing of calcium nitrate addition affects morphology, dispersity and composition of bioactive glass nanoparticles. *RSC Adv.* **6**, 95101–95111 (2016).
42. Y. Zhang, J. Luan, S. Jiang, X. Zhou, M. Li, The effect of amino-functionalized mesoporous bioactive glass on MC3T3-E1 cells in vitro stimulation. *Compos. Part B Eng.* **172**, 397–405 (2019).
43. C. Fiorica, G. Pitarresi, F. S. Palumbo, N. Mauro, S. Federico, G. Giammona, Production and physicochemical characterization of a new amine derivative of gellan gum and rheological study of derived hydrogels. *Carbohydr. Polym.* **236**, 116033 (2020).
44. H. J. Sim, T. Thambi, D. S. Lee, Heparin-based temperature-sensitive injectable hydrogels for protein delivery. *J. Mater. Chem. B* **3**, 8892–8901 (2015).
45. R. I. Sharma, J. G. Snedeker, Biochemical and biomechanical gradients for directed bone marrow stromal cell differentiation toward tendon and bone. *Biomaterials* **31**, 7695–7704 (2010).
46. A. Cipitria, K. Boettcher, S. Schoenhals, D. S. Garske, K. Schmidt-Bleek, A. Ellinghaus, A. Dienelt, A. Peters, M. Mehta, C. M. Madl, N. Huebsch, D. J. Mooney, G. N. Duda, In-situ tissue regeneration through SDF-1α driven cell recruitment and stiffness-mediated bone regeneration in a critical-sized segmental femoral defect. *Acta Biomater.* **60**, 50–63 (2017).
47. Z. Chen, J. Yuen, R. Crawford, J. Chang, C. Wu, Y. Xiao, The effect of osteoimmunomodulation on the osteogenic effects of cobalt incorporated β-tricalcium phosphate. *Biomaterials* **61**, 126–138 (2015).
48. S.-S. Jin, D.-Q. He, D. Luo, Y. Wang, M. Yu, B. Guan, Y. Fu, Z.-X. Li, T. Zhang, Y.-H. Zhou, C.-Y. Wang, Y. Liu, A biomimetic hierarchical nanointerface orchestrates macrophage polarization and mesenchymal stem cell recruitment to promote endogenous bone regeneration. *ACS Nano* **13**, 6581–6595 (2019).
49. M. Chen, Y. Zhang, P. Zhou, X. Liu, H. Zhao, X. Zhou, Q. Gu, B. Li, X. Zhu, Q. Shi, Substrate stiffness modulates bone marrow-derived macrophage polarization through NF-κB signaling pathway. *Bioact. Mater.* **5**, 880–890 (2020).
50. X.-D. Shi, L.-W. Chen, S.-W. Li, X.-D. Sun, F.-Z. Cui, H.-M. Ma, The observed difference of RAW264.7 macrophage phenotype on mineralized collagen and hydroxyapatite. *Biomed. Mater.* **13**, 041001 (2018).
51. Q. Huang, X. Li, T. A. Elkhooly, S. Xu, X. Liu, Q. Feng, H. Wu, Y. Liu, The osteogenic, inflammatory and osteo-immunomodulatory performances of biomedical Ti-Ta metal–metal composite with Ca- and Si-containing bioceramic coatings. *Colloids Surf. B Biointerfaces* **169**, 49–59 (2018).
52. X. Dong, J. Chang, H. Li, Bioglass promotes wound healing through modulating the paracrine effects between macrophages and repairing cells. *J. Mater. Chem. B* **5**, 5240–5250 (2017).

53. H. Kang, K. Zhang, D. S. H. Wong, F. Han, B. Li, L. Bian, Near-infrared light-controlled regulation of intracellular calcium to modulate macrophage polarization. *Biomaterials* **178**, 681–696 (2018).
54. R. Sridharan, B. Cavanagh, A. R. Cameron, D. J. Kelly, F. J. O'Brien, Material stiffness influences the polarization state, function and migration mode of macrophages. *Acta Biomater.* **89**, 47–59 (2019).
55. Y. Zhu, Z. Ma, L. Kong, Y. He, H. F. Chan, H. Li, Modulation of macrophages by bioactive glass/sodium alginate hydrogel is crucial in skin regeneration enhancement. *Biomaterials* **256**, 120216 (2020).
56. Y. Zhang, Y. Yan, X. Xu, Y. Lu, L. Chen, D. Li, Y. Dai, Y. Kang, K. Yu, Investigation on the microstructure, mechanical properties, in vitro degradation behavior and biocompatibility of newly developed Zn-0.8%Li-(Mg, Ag) alloys for guided bone regeneration. *Mater. Sci. Eng. C.* **99**, 1021–1034 (2019).
57. S. Zhang, Y. Guo, Y. Dong, Y. Wu, L. Cheng, Y. Wang, M. Xing, Q. Yuan, A novel nanosilver/nanosilica hydrogel for bone regeneration in infected bone defects. *ACS Appl. Mater. Interfaces* **8**, 13242–13250 (2016).
58. T. Sugimoto, M. Kanatani, J. Kano, H. Kaji, T. Tsukamoto, T. Yamaguchi, M. Fukase, K. Chihara, Effects of high calcium concentration on the functions and interactions of osteoblastic cells and monocytes and on the formation of osteoclast-like cells. *J. Bone Miner. Res.* **8**, 1445–1452 (1993).
59. N. Huebsch, E. Lippens, K. Lee, M. Mehta, S. T. Koshy, M. C. Darnell, R. M. Desai, C. M. Madl, M. Xu, X. Zhao, O. Chaudhuri, C. Verbeke, W. S. Kim, K. Alim, A. Mammoto, D. E. Ingber, G. N. Duda, D. J. Mooney, Matrix elasticity of void-forming hydrogels controls transplanted-stem-cell-mediated bone formation. *Nat. Mater.* **14**, 1269–1277 (2015).
60. P. Qiu, M. Li, K. Chen, B. Fang, P. Chen, Z. Tang, X. Lin, S. Fan, Periosteal matrix-derived hydrogel promotes bone repair through an early immune regulation coupled with enhanced angio- and osteogenesis. *Biomaterials* **227**, 119552 (2020).
61. M. J. Feito, R. Diez-Orejas, M. Cicuéndez, L. Casarrubios, J. M. Rojo, M. T. Portolés, Characterization of M1 and M2 polarization phenotypes in peritoneal macrophages after treatment with graphene oxide nanosheets. *Colloids Surf. B Biointerfaces.* **176**, 96–105 (2019).
62. H.-S. Moon, Y.-Y. Won, K.-D. Kim, A. Ruprecht, H.-J. Kim, H.-K. Kook, M.-K. Chung, The three-dimensional microstructure of the trabecular bone in the mandible. *Surg. Radiol. Anat.* **26**, 466–473 (2004).
63. J. C. M. Teo, K. M. Si-Hoe, J. E. L. Keh, S. H. Teoh, Correlation of cancellous bone microarchitectural parameters from microCT to CT number and bone mechanical properties. *Mater. Sci. Eng. C* **27**, 333–339 (2007).
64. J. Du, P. Xie, S. Lin, Y. Wu, D. Zeng, Y. Li, X. Jiang, Time-phase sequential utilization of adipose-derived mesenchymal stem cells on mesoporous bioactive glass for restoration of critical size bone defects. *ACS Appl. Mater. Interfaces* **10**, 28340–28350 (2018).
65. Q. Fu, E. Saiz, M. N. Rahaman, A. P. Tomsia, Bioactive glass scaffolds for bone tissue engineering: State of the art and future perspectives. *Mater. Sci. Eng. C* **31**, 1245–1256 (2011).
66. X. Chen, M. Wang, F. Chen, J. Wang, X. Li, J. Liang, Y. Fan, Y. Xiao, X. Zhang, Correlations between macrophage polarization and osteoinduction of porous calcium phosphate ceramics. *Acta Biomater.* **103**, 318–332 (2020).
67. J. T. Oliveira, T. C. Santos, L. Martins, R. Picciochi, A. P. Marques, A. G. Castro, N. M. Neves, J. F. Mano, R. L. Reis, Gellan gum injectable hydrogels for cartilage tissue engineering applications: In vitro studies and preliminary in vivo evaluation. *Tissue Eng. Part A* **16**, 343–353 (2010).

Acknowledgments

Funding: This work was supported by National Science Foundation of China (81771116 and 82001098) and Shanghai Sailing Program (19YF1425900). **Author contributions:** X.D. and J.S. (contributed equally): Conceptualization, methodology, validation, formal analysis, data curation, writing—original draft, and writing—review and editing. J.W.: Data curation and writing—review and editing. Y.L. and X.W.: Data curation and resources. Y.Z.: Resources. X.J.: Data curation. X.Z.: Data curation, writing—review and editing, project administration, and funding acquisition. H.L.: Conceptualization, supervision, writing—review and editing, project administration, and funding acquisition. **Competing interests:** The authors declare that they have no competing interests. **Data and materials availability:** All data needed to evaluate the conclusions in the paper are present in the paper and/or the Supplementary Materials.

Submitted 2 June 2021
Accepted 26 October 2021
Published 10 December 2021
10.1126/sciadv.abj7857